1 *Article*

2 # Reliability and Generalizability of Similarity-Based

3 # Fusion of MEG and fMRI Data in Human Ventral

4 # and Dorsal Visual Streams

5 **Yalda Mohsenzadeh [1, *], Caitlin Mullin [1, *], Benjamin Lahner [1, 2], Radoslaw Cichy [3]**
6 **and Aude Oliva [1]**

7 [1] Computer Science and AI Lab., MIT, Cambridge, MA, USA
8 [2] Boston University, Cambridge, MA, USA
9 [2] Free University Berlin, Berlin, Germany
10 * These authors contributed equally
11   Correspondence: yalda@mit.edu

12

13 **Abstract:** To build a representation of what we see, the human brain recruits regions throughout
14 the visual cortex in cascading sequence. Recently, an approach was proposed to evaluate the
15 dynamics of visual perception in high spatiotemporal resolution at the scale of the whole brain. This
16 method combined functional magnetic resonance imaging (fMRI) data with
17 magnetoencephalography (MEG) data using representational similarity analysis and revealed a
18 hierarchical progression from primary visual cortex through the dorsal and ventral streams. To
19 assess the replicability of this method, here we present results of a visual recognition neuro-imaging
20 fusion experiment, and compare them within and across experimental settings. We evaluated the
21 reliability of this method by assessing the consistency of the results under similar test conditions,
22 showing high agreement within participants. We then generalized these results to a separate group
23 of individuals and visual input by comparing them to the fMRI-MEG fusion data of Cichy et al
24 (2016), revealing a highly similar temporal progression recruiting both the dorsal and ventral
25 streams. Together these results are a testament to the reproducibility of the fMRI-MEG fusion
26 approach and allows for the interpretation of these spatiotemporal dynamic in a broader context.

27 **Keywords:** spatiotemporal neural dynamics; vision; dorsal and ventral streams; multivariate
28 pattern analysis; representational similarity analysis; fMRI; MEG

29

30 **1. Introduction**

31   To solve visual object recognition, the human brain has developed a particular cortical
32 topology within the ventral and dorsal streams, recruiting regions in cascading sequence, to quickly
33 build a representation of what we see (i.e. [1–9]).

34   To reveal the complex neural dynamics underlying visual object recognition, neural
35 responses must be resolved in both space and time simultaneously [10–15]. Towards this aim, Cichy
36 and collaborators proposed a novel approach to combine functional magnetic resonance imaging
37 (fMRI) with magnetoencephalography (MEG) termed MEG-fMRI fusion [8,9,16–18]. The results
38 revealed the dynamics of the visual processing cascade. Neural responses first emerge in the occipital
39 pole (V1, V2, V3) at around 80 msec, and then progress in the anterior direction along the ventral (i.e.
40 lateral-occipital cortex LO, ventral occipital cortex VO, temporal occipital cortex TO and

41 parahippocampal cortex PHC) and dorsal (intraparietal sulcus regions) visual streams within 110-
42 170 msec after image onset.

43 The consistency of these results with established findings [19–25] suggests that fMRI-MEG
44 fusion is an appropriate analytical tool to non-invasively evaluate the spatiotemporal mechanisms of
45 perception. To assess the power of the fusion technique to yield replicable results on visual
46 recognition dynamics in the human ventral and dorsal streams [26–28], here we replicate [9].
47 Specifically, we first evaluated the *reliability* of the fusion method at capturing the spatiotemporal
48 dynamics of visual perception by assessing the neural agreement of visually similar experiences
49 within individuals, asking: 'Do similar visual experiences obey similar spatiotemporal stages in the
50 brain?' Given the known variation across brain regions for separate visual category input (e.g. [1,29–
51 34]), our second objective was to determine the *generalizability* of these patterns: 'For a given task,
52 which spatiotemporal properties are reproducible across diverse visual input and independent
53 observer groups?'

2. Materials and Methods

55 This paper presents two independent experiments in which fMRI and MEG data were acquired
56 when observers look at pictures of natural images. The fMRI and MEG data of Experiment 1 are
57 original to this current work. Data of Experiment 2 has been published originally in [9] (Experiment
58 2).

2.1. Participants

60 Two separate groups of fifteen right-handed volunteers with normal or corrected to normal
61 vision participated in Experiment 1 (9 female, 27.87 ± 5.17 years old) and Experiment 2 (5 female, 26.6
62 ± 5.18 years old, see [9]). The participants signed an informed consent form and were compensated
63 for their participation. Both studies were conducted in accordance with the Declaration of Helsinki
64 and approved by the Institutional Review Board of Massachusetts Institute of Technology.

2.2. Stimulus Set

66 In Experiment 1, the stimulus set included *twin* sets of 78 real-world natural images each (156
67 images total). Twin-set 1 and Twin-set 2 each contained an image with the same verbal semantic
68 description (see Figure 1a, i.e. a pair of sunflowers, giraffes, horses, etc.). The sets were not
69 significantly different on a collection of low level image statistics [35,36]. The stimulus set of
70 Experiment 2 consisted of 118 natural images of objects [9] from the ImageNet dataset [37]. In both
71 experiments, participants performed the same orthogonal vigilance task. See Appendix A for details
72 on the Experimental Design.

2.3. fMRI and MEG Acquisition

74 MEG and fMRI data for Experiment 1 were acquired in separate sessions, similar to Experiment
75 2 in [9]. Images were presented 500 msec in all conditions. See Appendix B for data acquisition detail
76 of both experiments.

2.4. Data Analyses

78 We performed several data analyses to test the robustness and generalizability of our results.
79 First, we performed a *full brain fMRI-MEG fusion* [8,9,16,17], which uses representational similarity

analysis [38,39] to map MEG and fMRI data into a common space (see Appendix C for details). To summarize, the MEG data were analyzed in a time-resolved manner with 1 msec resolution. MEG sensor data at each time point were arranged in pattern vectors for each stimulus condition and repetition. These vectors were then used to train support vector machines to classify each pair of conditions. The performance of the binary SVM classifiers computed with leave-one-out cross validation procedure were interpreted as a pairwise dissimilarity measure (higher decoding indicates larger dissimilarity) and used to construct a condition by condition representational dissimilarity matrix (RDM) per time point (Figure 1b). The fMRI data were analyzed with a searchlight approach to construct the representational dissimilarity matrices in a voxel-resolved fashion. At every voxel in the brain, the condition-specific voxel patterns in its vicinity were extracted and pairwise condition-specific dissimilarities (1 - Pearson's R) were computed to create a condition by condition fMRI RDM assigned to that voxel (Figure 1c). Then, in the similarity space of RDMs, MEG and fMRI data were directly compared (Spearman's R) to integrate high spatial resolution of fMRI with high temporal resolution of MEG. In detail, for a given time point the MEG RDM was correlated with fMRI RDMs specified with the searchlight method resulting in a 3D correlation map. Repeating the procedure for all time points as depicted in Figure 1d resulted in a 4D spatiotemporal correlation map per individual. The correlation maps were averaged over individuals and significant correlations were determined with permutation tests and multiple comparison corrections over time and space with cluster correction method (N=15 in each experiment; cluster-definition threshold of 0.001 and cluster size threshold of 0.01). The detail on statistical tests are presented in Appendix E.

Second, to quantitatively compare the spatiotemporal neural dynamics within and across the experiments and show how reliable they are, we performed two types of anatomically-defined *region-of-interest (ROI) based analysis* along ventral and dorsal streams (see Appendix D for detail): 1) a *spatially restricted searchlight voxel-wise analysis*: in this analysis, the searchlight based MEG-fMRI fusion correlation time series are averaged over voxels within an ROI; 2) the conventional *ROI-based analysis*: in this analysis, the condition-specific voxel responses within an ROI are extracted, and the pairwise condition-specific response dissimilarities are computed to create an ROI RDM which is then compared with time-resolved MEG RDMs resulting in correlation time series (as in [9]).

3. Results

3.1. Reliability of similarity-based fMRI-MEG fusion method

We first assessed the reliability of the fMRI-MEG similarity-based data fusion method. For this we applied fMRI-MEG fusion separately to the two sets of images making up the Twins-set (i.e. Twin-set 1 and Twin-set 2) and compared the results.

Figure 2 and 3 show the spatiotemporal dynamics of visual perception in the ventral and dorsal visual pathways respectively for the Twins-sets over the time course of 1000 msec. Qualitatively examining these results reveal that the neural responses start in occipital pole around 70-90 msec after stimulus onset, followed by neural responses in anterior direction along the ventral stream (Figure 2ac), and across the dorsal stream up to the inferior parietal cortex (Figure 3ac).

118   To quantitatively compare the spatiotemporal fusion maps between the Twin-sets we performed
119   spatially restricted voxel-wise fMRI-MEG fusion on five regions-of-interest (ROIs) (early visual cortex
120   (EVC), ventral occipital area (VO), parahippocampal cortex (PHC), and inferior parietal sulci (IPS0
121   and IPS1). We averaged the correlation values over the voxels within each ROI resulting in one
122   correlation time series per individual. Figures 2b and 3b compare the ROI-specific time courses for
123   Twin-set 1 and 2. We observe that the two sets result in similar temporal dynamics within the regions
124   of interest across ventral and dorsal pathways (All statistical tests are performed using permutation
125   tests with cluster defining threshold P<0.01, and corrected significance level P<0.01; n=15). This
126   demonstrates the reliability of the fusion method in reproducing similar patterns across similar visual
127   experiences.

128   Next, we performed an ROI-based fMRI-MEG fusion following the method described in [8,9]
129   (see Figure 4a). Studied ROIs (see details in Appendix D) include EVC, ventral regions (VO, TO, PHC)
130   and dorsal regions (IPS0, IPS1, IPS2, and IPS3). As depicted in Figure panels 4bcde, the ROI-based
131   fMRI-MEG fusion results in visually similar time series. Comparison of peak latency times show a
132   peak of response around 120 msec in EVC and significantly later (two-sided hypothesis test, all
133   P<0.01, FDR corrected), around 140 msec in ventral and dorsal ROIs. The peak latency and onset
134   times with their corresponding 95% confidence intervals are reported in Table 1.

135   *3.2. Generalizability of similarity-based fMRI-MEG fusion method*

136   We evaluated the generalizability of the fMRI-MEG similarity-based data fusion method by
137   comparing results across participant groups presented with different images (Twins-Set and
138   ImageNet-Set from Experiment 2 of [9]). We applied the fMRI-MEG similarity-based data fusion
139   method to Twins-set and ImageNet-set, separately. Figures 5 and 6 display the spatiotemporal
140   dynamics of visual perception for the two datasets along the ventral and dorsal visual pathways,
141   respectively, over the first 1000 msec from stimulus onset. In both cases, the significant signals emerge
142   in EVC around 70-80 msec after stimulus onset and and then in the anterior direction along the
143   ventral stream (Figure 5ac), and across the dorsal stream up to the inferior parietal cortex (Figure
144   6ac). We determined significant spatiotemporal correlations with sign-permutation tests (n=15; P <
145   0.01 cluster-definition threshold, P < 0.001 cluster threshold).

146   Figures 5b and 6b show qualitatively similar patterns of spatiotemporal fusion maps between
147   the two datasets (Twins-Set and ImageNet-Set) by averaging the correlations over the voxels
148   (spatially restricted voxel-wise fMRI-MEG fusion) in EVC, ventral regions (VO and PHC) and dorsal
149   regions (IPS0 and IPS1).

150   To further investigate the similarities and dissimilarities between these two sets of data
151   quantitatively, we performed ROI-based analyses. For each dataset, we correlated ROI-specific fMRI
152   RDMs with time-resolved MEG RDMs resulting in correlation time courses shown in Figure 7abcd.
153   We determined significant time points illustrated with color coded lines below the graphs with sign-
154   permutation tests (n=15; P < 0.01 cluster-definition threshold, P < 0.01 cluster threshold). We observed
155   that in both datasets, correlation time series peak significantly earlier in EVC compared to high level
156   regions in ventral (VO and PHC) and dorsal (IPS0, IPS1, IPS2) pathways (two-sided hypothesis test,
157   all P<0.01, FDR corrected) reflecting the established structure of the visual hierarchy. Peak and onset

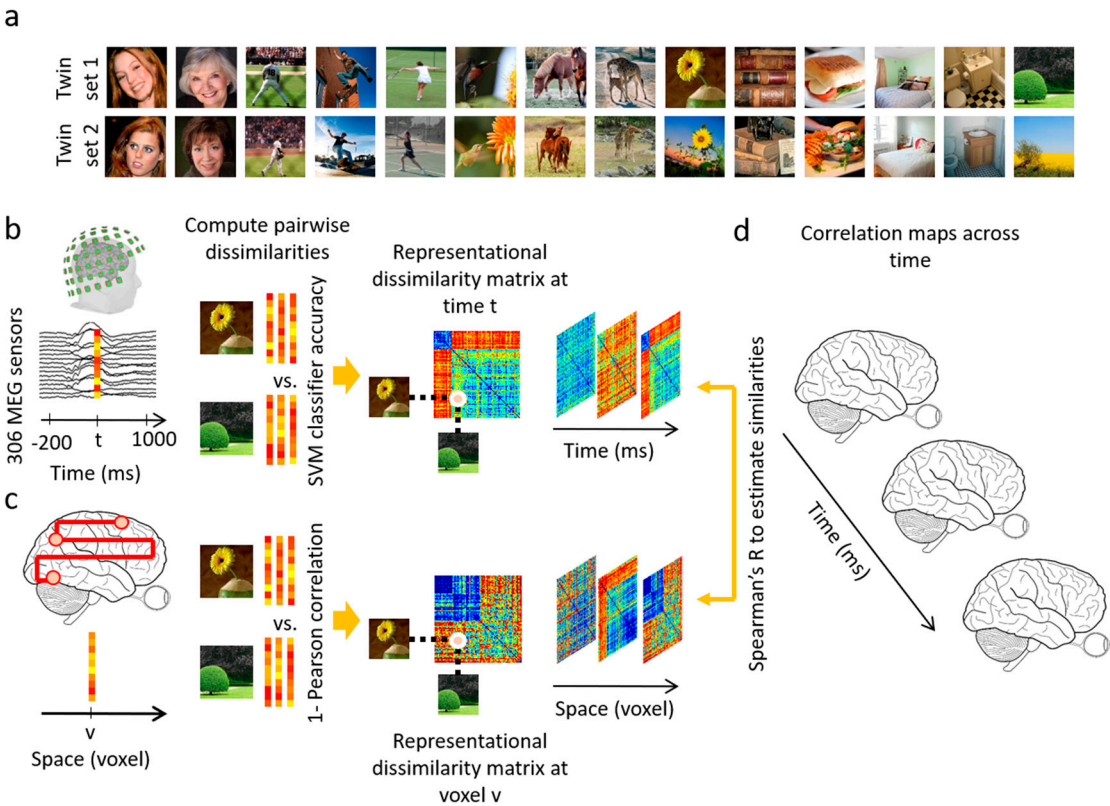158   latencies of curves in Figure 7abcd and their corresponding 95% confidence intervals are reported in
159   Table 2.

160

161   **Figure 1.** Examples of stimuli of Experiment 1 and analysis scheme: (**a**) Examples of experimental
162   condition: The stimulus set consisted of two sets (termed *twin-sets 1 and 2*) of 78 object images each ordered
163   in pairs, such that each set was of the same semantic content but different in appearance. (**b**) MEG
164   multivariate analysis. MEG data were extracted from -200 msec to 1000 msec with respect to stimulus onset.
165   The 306 dimensional MEG sensor data at each time point t were arranged in vectors. For each pair of
166   conditions, the performance of a SVM classifier in discriminating the conditions based on vector patterns
167   was used as a measure of dissimilarity between the pair of conditions. A representational dissimilarity
168   matrix at each time point t was populated using these pairwise dissimilarities; (**c**) fMRI multivariate
169   analysis. At each voxel v, the activation patterns in a sphere with radius of 4 voxels were extracted and
170   pairwise dissimilarities of conditions were computed (1-Pearson's R) yielding a representational
171   dissimilarity matrix assigned to the voxel v at the center of the sphere; (**d**) fMRI-MEG similarity based
172   fusion. The MEG RDM representation at each time point t were compared with the fMRI RDM
173   representations at each voxel v by computing Spearman's R correlations. These computations resulted in
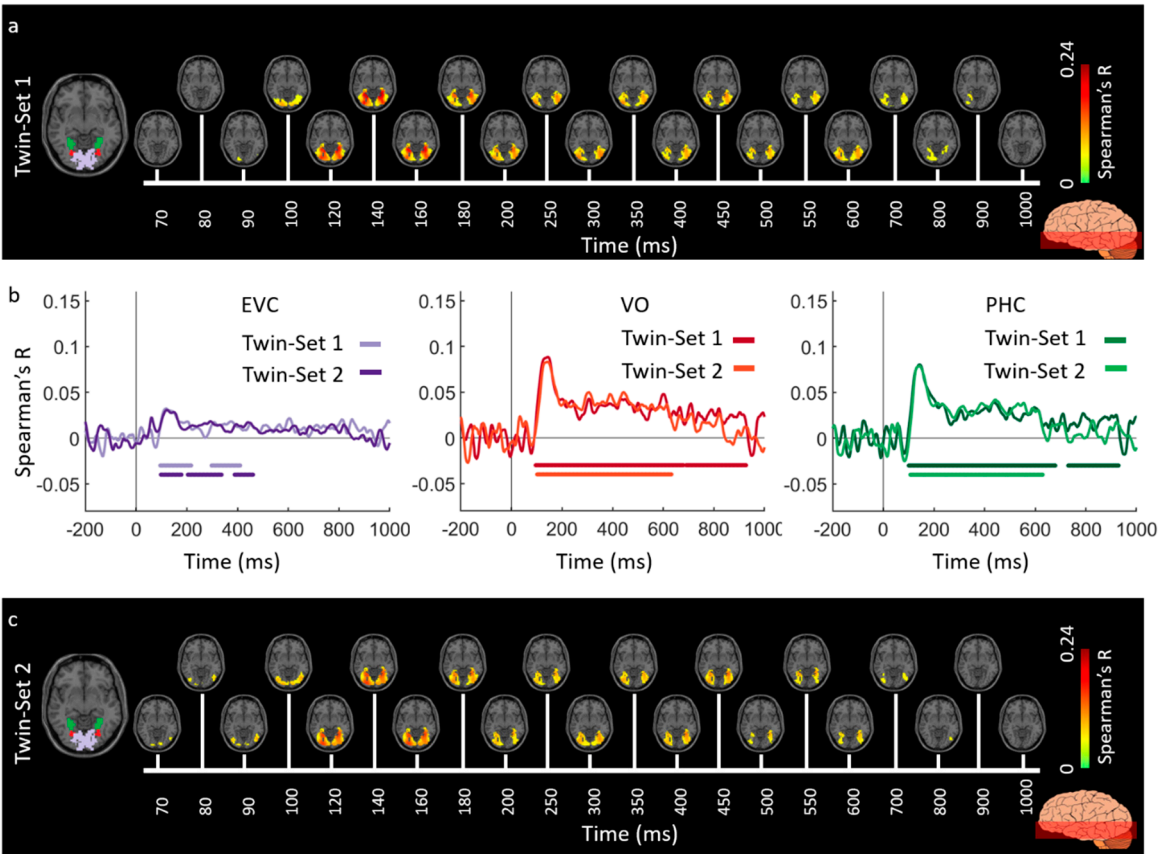174   correlation maps over the whole brain and across time.

Figure 2. Experiment 1 Twins-set spatiotemporal neural dynamics of vision in ventral stream: (**a**) An axial slice encompassing early visual cortex (EVC) and ventral ROIs, ventral occipital (VO) area and parahippocampal cortex (PHC). The significant correlation maps for Twin-set 1 in this axial slice depicted over time (n = 15, cluster-definition threshold P < 0.001, cluster threshold P < 0.01); (**b**) The correlation time series are computed based on spatially restricted searchlight voxel-wise fusion analysis (see Methods). The depicted curves from left to right compare these time series in EVC and ventral ROIs VO and PHC for Twin-set 1 and Twin-set 2. Significant time points depicted with color coded lines below the graphs are determined with sign-permutation tests (n=15; P < 0.01 cluster-definition threshold, P < 0.01 cluster threshold); (**c**) The significant correlation maps for Twin-set 2 in the same axial slice as (a) depicted over time (n = 15, cluster-definition threshold P < 0.001, cluster threshold P < 0.01).
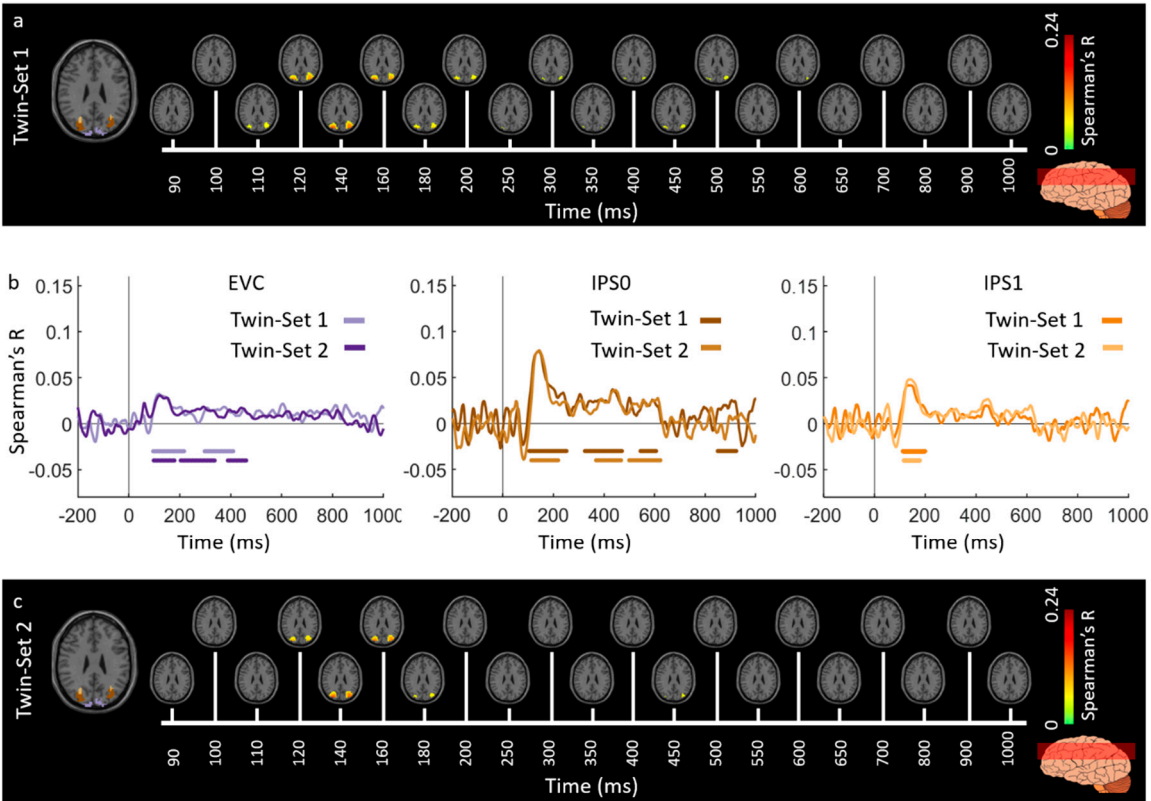
Figure 3. Experiment 1 Twins-set spatiotemporal neural dynamics of vision in dorsal stream: (**a**) An axial slice encompassing early visual cortex (EVC) and dorsal ROIs, inferior parietal sulcus (IPS0 and IPS1). The significant correlation maps for Twin-set 1 in this axial slice depicted over time (n = 15, cluster-definition threshold P < 0.001, cluster threshold P < 0.01); (**b**) The correlation time series are computed based on spatially restricted searchlight voxel-wise fusion analysis (see Methods). The depicted curves from left to right compare these time series in EVC and dorsal ROIs, IPS0 and IPS1 for Twin-set1 and Twin-set2. Significant time points depicted with color coded lines below the graphs are determined with sign-permutation tests (n=15; P < 0.01 cluster-definition threshold, P < 0.01 cluster threshold); (**c**) The significant correlation maps for Twin-set 2 in the same axial slice as (a) depicted over time (n = 15, cluster-definition threshold P < 0.001, cluster threshold P < 0.01).
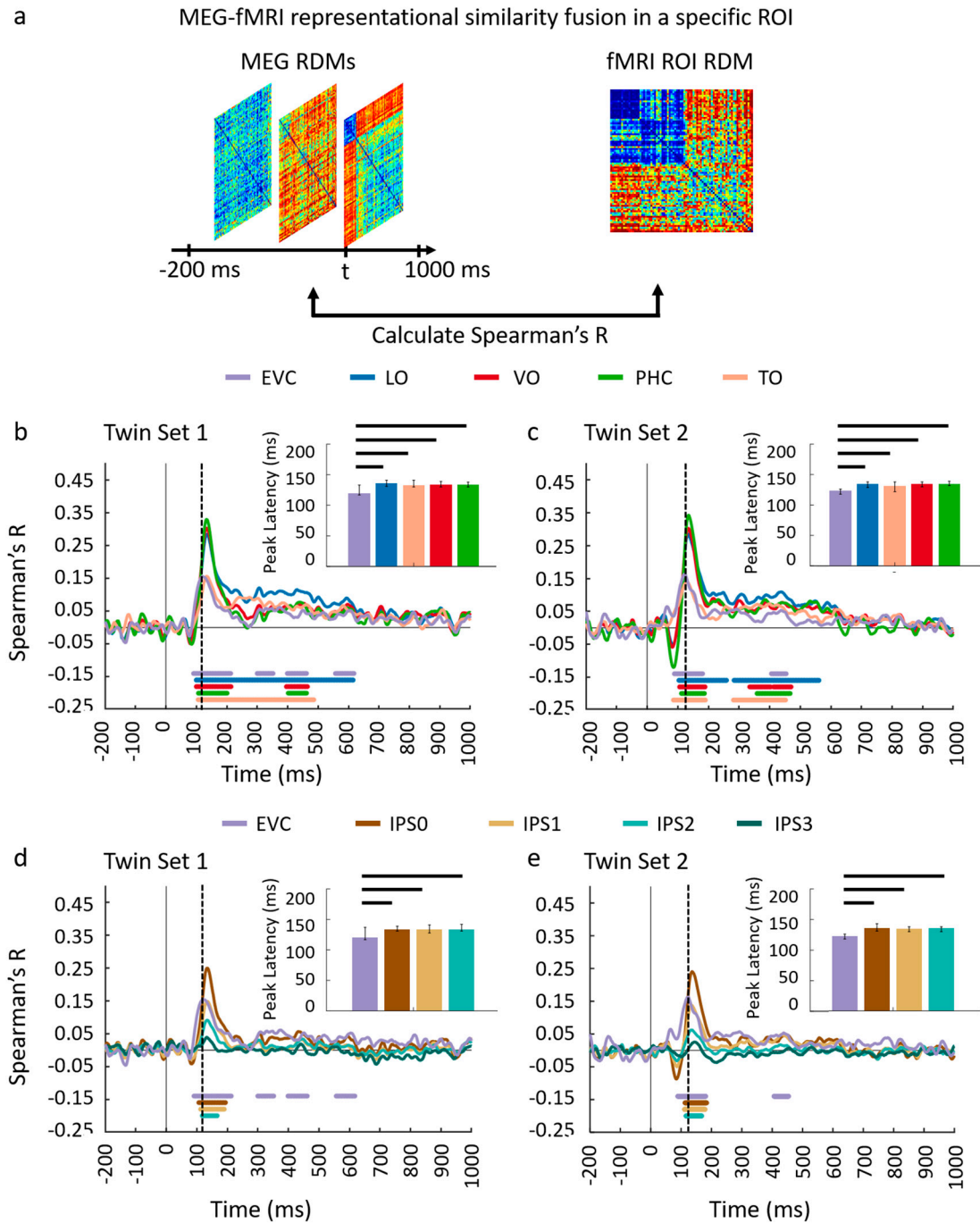
Figure 4. Comparing dorsal and ventral stream neural responses through similarity-based ROI fMRI-MEG fusion. (**a**) The voxel patterns are extracted from each ROI to construct the fMRI ROI RDM. Then the ROI-specific fMRI RDM was compared with time-resolved MEG RDMs resulting in correlation time series for each region of interest; (**bc**) The fMRI-MEG fusion time series are depicted in EVC and ventral ROIs, LO, VO, PHC, and TO for Set 1 and 2, respectively; (**de**) The fMRI-MEG fusion time series are depicted in EVC and dorsal ROIs, IPS0-3 for Twin-set 1 and Twin-set 2, respectively. The color coded lines below the curves indicate significant time points (n = 15, cluster-definition threshold P < 0.01, cluster threshold P < 0.01) and the dashed vertical line in each plot indicates the peak latency in EVC time series. Peak latency times and their corresponding 95% confidence intervals for correlation time series in bcde are illustrated with barplots and error bars, respectively. Black lines

208   above the bar indicate significant differences between conditions. 95% confidence intervals were
209   found with bootstrap tests and barplots were evaluated with two-sided hypothesis tests; false
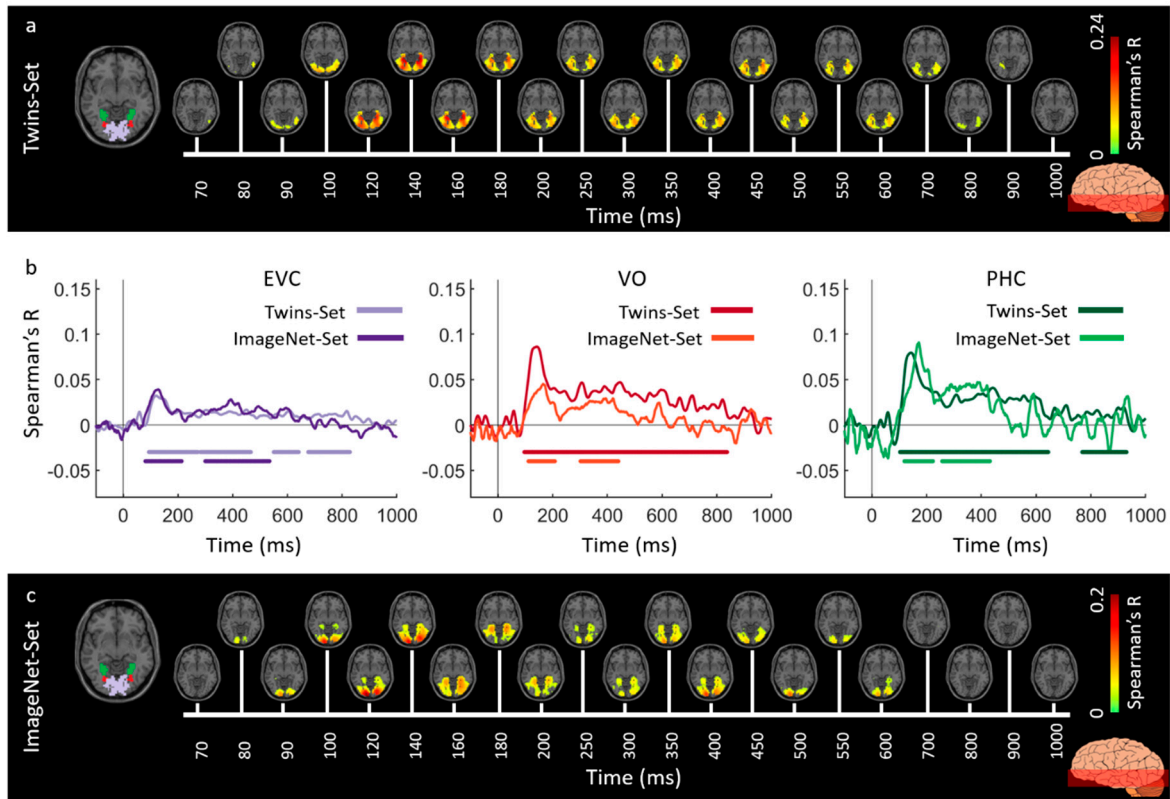210   discovery rate corrected at P<0.05.

211
212   **Figure 5.** Spatiotemporal neural dynamics of vision in ventral stream: (**a**) An axial slice encompassing
213   early visual cortex (EVC) and ventral ROIs, occipital (VO) area and parahippocampal cortex (PHC).
214   The significant correlation maps for Twins-set (Experiment 1) in this axial slice depicted over time (n
215   = 15, cluster-definition threshold P < 0.001, cluster threshold P < 0.01); (**b**) The correlation time series
216   are computed based on spatially restricted searchlight voxel-wise fusion analysis (see Methods). The
217   depicted curves from left to right compare these time series in EVC and ventral ROIs VO and PHC
218   for Twins-set (Experiment 1) and ImageNet-set (Experiment 2). Significant time points depicted with
219   color coded lines below the graphs are determined with sign-permutation tests (n=15; P < 0.01 cluster-
220   definition threshold, P < 0.01 cluster threshold); (**c**) The significant correlation maps for ImageNet-set
221   (Experiment 2) in the same axial slice as (a) depicted over time (n = 15, cluster-definition threshold P
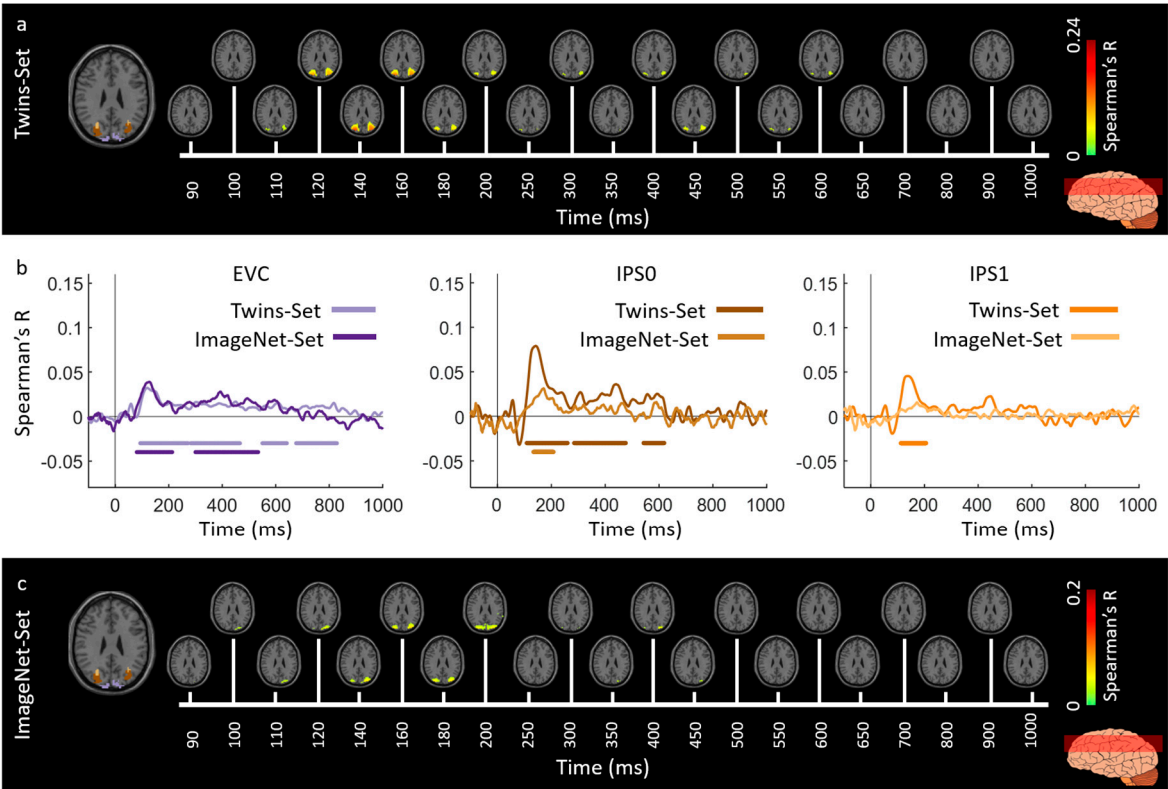222   < 0.001, cluster threshold P < 0.01).

Figure 6. Spatiotemporal neural dynamics of vision in dorsal stream: (**a**) An axial slice encompassing early visual cortex (EVC) and dorsal ROIs, inferior parietal sulcus (IPS0 and IPS1). The significant correlation maps for Twins-set (Experiment 1) in this axial slice depicted over time (n = 15, cluster-definition threshold P < 0.001, cluster threshold P < 0.01); (**b**) The correlation time series are computed based on spatially restricted searchlight voxel-wise fusion analysis (see Methods). The depicted curves from left to right compare these time series in EVC and dorsal ROIs, IPS0 and IPS1 for Twins-set (Experiment 1) and ImageNet-set (Experiment 2). Significant time points depicted with color coded lines below the graphs are determined with sign-permutation tests (n=15; P < 0.01 cluster-definition threshold, P < 0.01 cluster threshold); (**c**) The significant correlation maps for ImageNet-set (Experiment 2) in the same axial slice as (a) depicted over time (n = 15, cluster-definition threshold P < 0.001, cluster threshold P < 0.01).
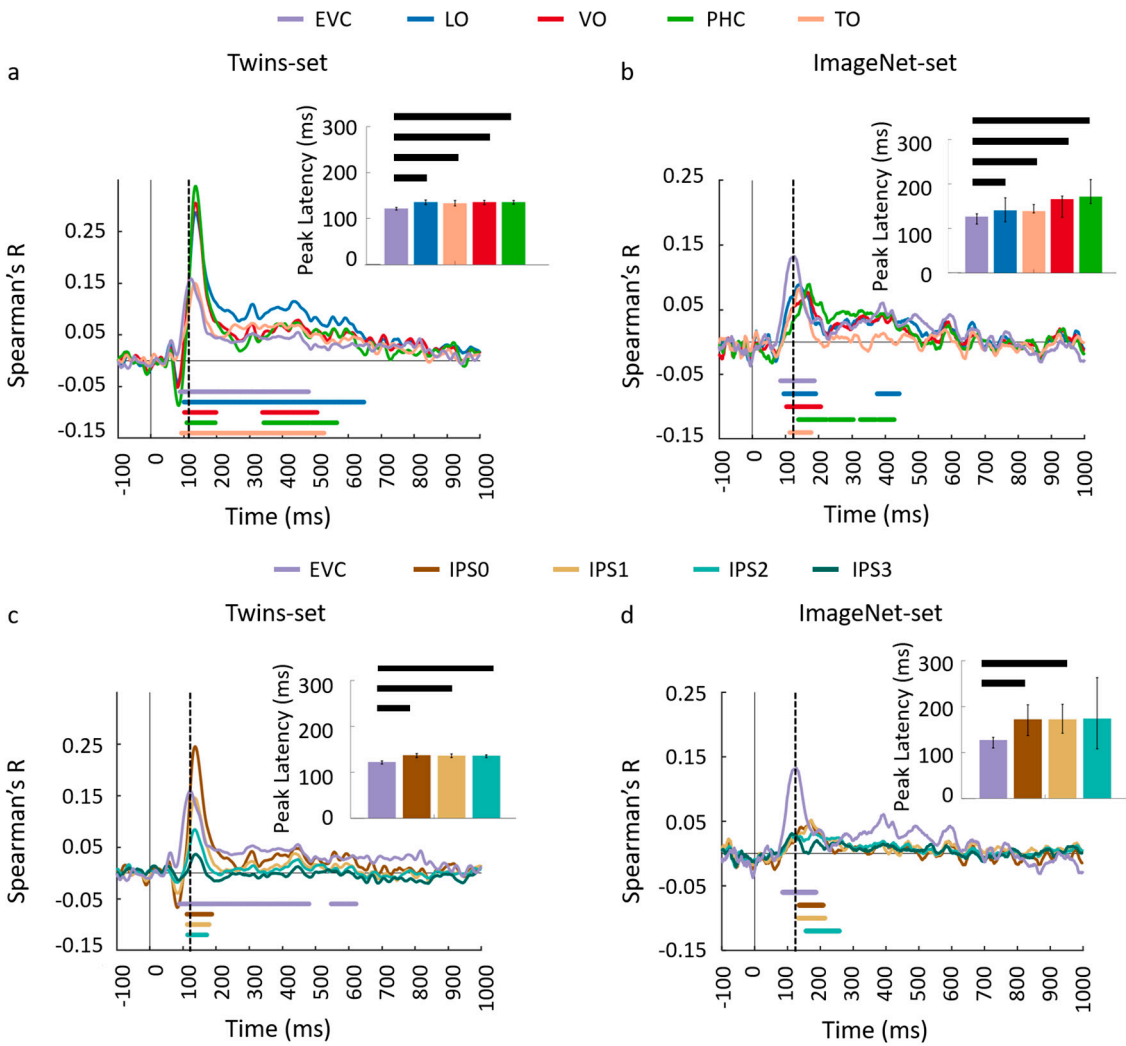
236

237

Figure 7. Comparing dorsal and ventral stream neural responses through similarity-based ROI fMRI-MEG fusion. The voxel patterns are extracted from each ROI to construct the fMRI ROI RDM. Then the ROI-specific fMRI RDM was compared with time-resolved MEG RDMs resulting in correlation time series for each region of interest; (**ab**) The fMRI-MEG fusion time series are depicted in EVC and ventral ROIs, LO, VO, PHC, and TO for Twins-set and ImageNet-set, respectively; (**cd**) The fMRI-MEG fusion time series are depicted in EVC and dorsal ROIs, IPS0-3 for Twins-set and ImageNet-set, respectively. The color coded lines below the curves indicate significant time points (n = 15, cluster-definition threshold $P < 0.01$, cluster threshold $P < 0.01$) and the dashed vertical line in each plot indicates the peak latency in EVC time series. Peak latency times and their corresponding 95% confidence intervals for correlation time series in bcde are illustrated with barplots and error bars, respectively. Black lines above the bar indicate significant differences between conditions. 95% confidence intervals were found with bootstrap tests and barplots were evaluated with two-sided hypothesis tests; false discovery rate corrected at $P<0.05$.

251

Table 1. Peak and onset latency for fMRI-MEG fusion time series in EVC, ventral, and dorsal regions for Twin-Set 1 and Twin-Set 2 (Experiment 1).

Region of Interest	Twin-Set 1		Twin-Set 2	
	Peak latency (ms)	Onset latency (ms)	Peak latency (ms)	Onset latency (ms)
EVC	120 (117-137)	92 (85-99)	123 (118-126)	90 (51-94)
Dorsal regions				
IPS0	134 (131-139)	107 (97-116)	136 (131-143)	113 (107-118)
IPS1	134 (128-141)	113 (102-123)	135 (130-138)	111 (105-116)
IPS2	134 (131-142)	118 (95-156)	136 (130-138)	116 (107-126)
Ventral regions				
LO	136 (131-141)	101 (95-107)	134 (129-138)	105 (100-108)
VO	134 (130-139)	100 (95-105)	135 (130-138)	104 (99-111)
TO	133 (130-141)	104 (92-111)	131 (122-138)	85 (73-101)
PHC	134 (130-138)	106 (99-113)	135 (132-139)	112 (107-116)

Values are averaged over n=15 subjects with 95% confidence intervals reported in parentheses.

Table 2. Peak and onset latency for fMRI-MEG fusion time series in EVC, ventral, and dorsal regions for Twins-Set (Experiment 1) and ImageNet-Set (Experiment 2).

Region of Interest	Twins-Set		ImageNet-Set	
	Peak latency (ms)	Onset latency (ms)	Peak latency (ms)	Onset latency (ms)
EVC	122 (119-125)	89 (56-95)	127 (110-133)	84 (71-91)
Dorsal regions				
IPS0	137 (131-141)	111 (102-117)	172 (137-204)	133 (99-156)
IPS1	136 (132-140)	111 (103-119)	172 (142-205)	137 (99-158)
IPS2	136 (132-138)	112 (100-119)	174 (108-263)	103 (90-186)
Ventral regions				
LO	136 (131-141)	102 (97-107)	141 (115-169)	96 (87-118)
VO	136 (131-139)	102 (95-109)	166 (125-173)	103 (95-125)
TO	134 (128-140)	90 (77-100)	139 (135-154)	115 (95-126)
PHC	136 (132-139)	109 (102-115)	172 (156-210)	121 (99-159)

Values are averaged over n=15 subjects with 95% confidence intervals reported in parentheses.

4. Discussion

One of the central tenants of science is reproducibility [40–42]. This is especially relevant in cognitive neuroscience, as the surge of new cutting-edge multivariate analysis tools has made it possible to address questions that were previously untestable [38,43]. Here, we have demonstrated the reproducibility of the fMRI-MEG fusion method through the application of two separate experiments, testing the reliability and generalizability of the technique.

The first analysis compared neural data within the same subject groups across Twin image sets, with equalized low-level visual features, and sharing highly similar semantic concepts (e.g. a giraffe for a

266 giraffe, a flower for a flower). We observed that the analysis yielded *reliably* consistent spatiotemporal
267 dynamics, with each subset showing responses first in the occipital pole, and then signals in the
268 anterior direction, with similar path in both ventral and dorsal streams. The strong agreement
269 between the full brain spatiotemporal maps of the Twin-sets suggests that the signals detected by the
270 fMRI-MEG data fusion method is likely to reliably reflect the representations of the stimulus. This
271 sequence of representational signals followed the established spatial [44,45] and temporal [19,46]
272 patterns associated with hierarchical visual processing.

273 This high degree of reliability, within subjects, across these separate but matched image-sets has
274 pragmatic consequences in reinforcing the power and confidence of this method. The agreement
275 within results of unimodal neuro-imaging have been shown have low test-retest reliability [28]. This
276 realization has brought about a crisis of confidence in the replicability and reliability of published
277 research findings within neuroscience [47,48]. Thus to mitigate these concerns the generation of new
278 research discoveries requires that findings move beyond drawing conclusions solely on the basis of
279 a single study. As such, we sought to extend this replication by comparing the newly collected Twins-
280 Set data to previously published independent fMRI-MEG fusion data [9]. This analysis focused on
281 the generalizability of this method across subject groups and to a wider range of stimuli.

282 Across the two experiments, findings from the full brain correlation maps and spatially restricted
283 ROI analysis revealed that the fMRI-MEG data fusion captures the spatiotemporal dynamic patterns
284 common to visual processing in a manner that *generalizes* across subjects and natural images. The
285 results of both experiments illustrate the spatiotemporal progression associated with hierarchical
286 visual processing [6,49,50], with significant signals emerging first in early visual areas and then along
287 the ventral and dorsal pathways.

288 We found that overall this generalized response had similar expected spatiotemporal response
289 patterns, but with greater variability in high-level visual areas. Previous work examining the
290 replicability of neuroimaging data has shown that low-level brain functions (motor and sensory
291 tasks), show generally less variance than high level cognitive tasks [51]. Moreover, between subject
292 comparisons show significantly higher variability than within due to the increase sources of noise
293 [52].

294 Cognitive neuroscientists have many methodological options for studying how experimental
295 variables are systematically related to the spatiotemporal dynamics underlying a cortical process of
296 interest. To date, much of our understanding has been advanced by methods that yield high spatial
297 or temporal resolution, but not both. Separately, the limitations of these modalities in their
298 application to understanding cognition are well known. Here we show that combining these methods
299 through representational similarity analysis provides a reliable and generalizable tool for studying
300 visual perception. This confirmatory replication within and between image-sets and subject-groups
301 provides a spatiotemporal dynamic map of visual processing that can act as a guideline for further
302 questions regarding the interactions between visual perception and cognitive factors, such as
303 attention and memory.

304

Appendix A

Experimental Design: In both experiments, images were presented at the center of the screen for 500 msec with 6 and 4 degrees of visual angle in Experiment 1 and 2, respectively. The task was the same for both experiments: the images were overlaid with a black fixation cross at the center and participants performed an orthogonal vigilance task. The data were collected over one MEG session and two fMRI sessions in both experiments.

MEG session included 25 runs for Experiment 1 and 15 runs for Experiment 2. Images were presented once per run in randomized order with 1-1.2 sec stimulus onset asynchrony (SOA) in Experiment 1 and twice per run with 0.9-1 sec OSA in Experiment 2. The participants were instructed to press a button and make an eye blink upon detection of a specific image (depicting an eye in Experiment 1 and a paper clip in Experiment 2) presented every 3-5 trials randomly.

The two fMRI sessions consisted of 11-15 runs in Experiment 1 and 9-11 runs in Experiment 2. Images were presented once per run in random order. In both studies 39 null trials were randomly distributed in each run. During the null trials the fixation cross changed color for 100 msec and subjects were instructed to respond to this color change by pressing a button. The trial duration was 3 sec in both studies. Images were presented for 500 msec and stimulus onset asynchrony was 3 sec, or 6 sec (if a preceding null trial).

Appendix B

MEG Acquisition and Analysis

MEG data were acquired from a 306-channel Elekta neuromag TRIUX system with sampling rate of 1 kHz and filtered by a 0.03 to 330 Hz band-pass filter. Participants' head position was measured prior and during the recording with 5 coils attached to their head. A maxfilter was applied for temporal source space separation and correcting for head movements [53,54]. Data were analyzed using Brainstorm software [55] to extract trials from -200 msec to 1000 msec with respect to image onset in Experiment 1 and from -100 msec to 1000 msec relative to image onset in Experiment 2. The mean of the baseline was removed and the data were smoothed with a 30 Hz low-pass filter. For each condition and participant, we obtained 25 trials in Experiment 1 and 30 trials in Experiment 2.

344   Multivariate pattern analysis was used to determine the similarity relations between visual
345   conditions (Figure 1b). At each time point t, MEG sensor data were arranged in pattern vectors
346   resulting in N vectors per condition at that time point with N being the number of trials per condition.
347   Then, for each pair of conditions a support vector machine (SVM) classifier was trained to
348   discriminate the conditions based on the MEG pattern vectors at each time point. The performance
349   of the classifier computed with leave-one-out cross validation procedure was considered as a
350   measure of dissimilarity between those pairs of conditions and used to construct a C x C (C=156 in
351   Experiment 1 and C=118 in Experiment 2) representational dissimilarity matrix (RDM) at each time
352   point. Each row and column in this matrix are indexed by a specific condition (image) and each matrix
353   entry shows how dissimilar the corresponding conditions are based on the MEG signals at a specific
354   time point. These matrices are symmetric with an undefined diagonal. To overcome computational
355   complexity and reduce noise, trials were randomly sub-averaged in groups of 3 in Experiment 1, and
356   groups of 5 in Experiment 2, before entering them into multivariate analysis.

357   *fMRI Acquisition and Analysis*

358   The MRI data of both experiments were acquired with a 3T Trio Siemens scanner using a 32-
359   channel head coil. The structural images were acquired using a standard T1-weighted sequence (192
360   sagittal slices, FOV = 256 mm2 , TR = 1900 msec, TE = 2.52 msec, flip angle = 9°).

361   Functional data of Experiment 1 was acquired over 11-15 runs of 305 volumes in two sessions
362   with gradient-echo EPI sequence: TR =2000 msec, TE = 29 msec, flip angle = 90°, FOV read = 200 mm,
363   FOV phase = 100%, bandwidth 2368 Hz/Px, resolution = 3 mm3 , slice gap 20%, slices = 33, ascending
364   interleaved acquisition). Functional data of Experiment 2 was acquired over 9-11 runs of 648 volumes
365   in two sessions with gradient-echo EPI sequence: TR =750 msec, TE = 30 msec, flip angle = 61°, FOV
366   read = 192 mm, FOV phase = 100% with a partial fraction of 6/8, through-plane acceleration factor 3,
367   bandwidth 1816 Hz/Px, resolution = 3 mm3 , slice gap 20%, slices = 33, ascending interleaved
368   acquisition).

369   The fMRI data in both studies were preprocessed using SPM software. For each participant,
370   fMRI data were slice-time corrected, realigned and co-registered to the T1 structural scan of the first
371   session, and finally normalized to the standard MNI space. We applied a general linear model (GLM)
372   to estimate the fMRI responses to the 156 and 118 image conditions in Experiment 1 and 2,
373   respectively. Stimulus onsets and durations, as well as motion and run regressors were included in
374   the GLM. All the regressors were convolved with a hemodynamic response function (canonical HRF)
375   with time resolution of TR/N and onset of the first slice (TR = 2000 msec, N = 33 slices). By contrasting
376   each condition against the implicit baseline, we converted the condition-specific GLM estimates into
377   t-value maps (resulting in 156 condition-specific t-maps for Experiment 1 and 118 condition-specific
378   t-maps for Experiment 2).

379   We then applied the searchlight analysis method to create the fMRI RDMs [56,57] for each
380   subject, separately. At each voxel v, condition-specific t-value pattern vectors were extracted in a
381   sphere centered at voxel v with a 4-voxel radius. Dissimilarities between these pattern vectors were
382   computed in a pairwise manner (1-Pearson's R). Then these dissimilarities were entered into an RDM
383   matrix in which its rows and columns were indexed by the image conditions. This process resulted

384   in a 156 x 156 RDM at each voxel for fMRI data of each subject in Experiment 1 and a 118 x 118 RDM
385   at each voxel for fMRI data of each subject in Experiment 2.

Appendix C

387   *Full Brain fMRI-MEG Fusion:* The assumption in the fusion analysis is that the pairwise condition-
388   specific relations (in the form of RDM representations) are preserved across MEG and fMRI data
389   patterns. For example, if two images result in similar patterns in MEG data, they produce similar
390   patterns in fMRI data as well. Comparison of pairwise similarity relations across MEG and fMRI
391   makes it possible to relate representations at specific time points (in MEG) with specific locations (in
392   fMRI). For both datasets, we performed within subject analysis comparing averaged MEG RDMs
393   over the 15 subjects, with subject-specific fMRI RDMs. We computed the correlations (Spearman's R)
394   between MEG RDMs at each time point and fMRI RDMs at each voxel. These computations resulted
395   in a 3D correlation map over the whole brain at each time point. Repeating the analysis over time
396   yielded a spatiotemporally resolved view of visual information in the brain.

Appendix D

Region-of-Interest Analysis

399   *Spatially Restricted Searchlight Voxel-wise fMRI-MEG Fusion*: This analysis followed the regular voxel-
400   wise full brain fMRI-MEG fusion but in spatially restricted regions of the brain. In detail, the search-
401   light method was performed within the ROI and an RDM matrix was created at each specific voxel
402   by comparing condition-specific fMRI pattern responses within the searchlight sphere centered at
403   the voxel (1-Pearson's R). Then the time-resolved MEG RDMs were compared with these fMRI
404   RDMs (Spearman's R) resulting in correlation time series within the ROI which were then averaged
405   resulting in one correlation time-course per ROI and per subject. This ROI analysis method is
406   directly comparable with the full brain fusion analysis and it is a convenient way to quantitatively
407   compare the spatiotemporal dynamics of fusion movies within specific brain regions.

408   *ROI-based fMRI-MEG Fusion*: This analysis method followed [8,9]. We extracted the voxel patterns
409   within each ROI and then computed the condition-specific pairwise dissimilarities (1-Pearson's R)
410   to create a single RDM matrix per ROI. Thus we obtained one fMRI RDM for each ROI per subject.
411   The fMRI ROI RDMs were averaged over subjects and then compared with subject-specific MEG
412   RDMs over time by computing their Spearman's R correlations. This process results in time-course
413   of MEG-fMRI fusion in each ROI per subject.

414   Specifically, we extracted the following ROIs: one early visual cortex (combining V1, V2, V3),
415   four ventral visual areas (lateral occipital (LO1&2), temporal occipital (TO), ventral occipital
416   (VO1&2), and parahippocampal cortex (PHC1&2) and four parietal areas (intraparietal cortex
417   including IPS0, IPS1, IPS2, and IPS3). The ROI definition followed [9] based on the probabilistic maps
418   of [58].

Appendix E

Statistical Testing

For statistical inference, we used non-parametric statistical tests [59,60] assessed by permutation-based cluster-size inference. The null hypothesis was zero for MEG-fMRI correlation time series and 4D spatiotemporal correlation maps. In all cases, we used 1000 permutations, 0.01 cluster defining threshold and 0.01 cluster threshold for time series; and 0.001 cluster defining threshold and 0.01 cluster threshold for 4D maps.

For peak and onset latency of the time series statistical assessments, bootstrap tests were performed. We bootstrapped the subject-specific time series for 1000 times to estimate an empirical distribution over peak and onset latency of the subject-averaged time courses and use it to define 95% confidence intervals. For peak to peak latency comparisons, 1000 bootstrapped samples of two peak differences were obtained. The null hypothesis was rejected if the 95% confidence interval of the peak latency differences did not include zero.

References

1. Malach, R.; Reppas, J. B.; Benson, R. R.; Kwong, K. K.; Jiang, H.; Kennedy, W. A.; Ledden, P. J.; Brady, T. J.; Rosen, B. R.; Tootell, R. B. Object-related activity revealed by functional magnetic resonance imaging in human occipital cortex. *Proc. Natl. Acad. Sci.* **1995**, *92*, 8135–8139, doi:10.1073/pnas.92.18.8135.

2. Grill-Spector, K.; Kourtzi, Z.; Kanwisher, N. The lateral occipital complex and its role in object recognition. *Vision Res.* **2001**, *41*, 1409–1422, doi:10.1016/S0042-6989(01)00073-6.

3. Johnson, J. S.; Olshausen, B. A. Timecourse of neural signatures of object recognition. *J. Vis.* **2003**, *3*, 4, doi:10.1167/3.7.4.

4. Op de Beeck, H. P.; Baker, C. I. The neural basis of visual object learning. *Trends Cogn. Sci.* **2010**, *14*, 22–30, doi:10.1016/j.tics.2009.11.002.

5. Mullin, C. R.; Steeves, J. K. E. Consecutive TMS-fMRI Reveals an Inverse Relationship in BOLD Signal between Object and Scene Processing. *J. Neurosci.* **2013**, *33*, 19243–19249, doi:10.1523/JNEUROSCI.2537-13.2013.

6. DiCarlo, J. J.; Zoccolan, D.; Rust, N. C. How Does the Brain Solve Visual Object Recognition? *Neuron* **2012**, *73*, 415–434, doi:10.1016/j.neuron.2012.01.010.

7. Konkle, T.; Oliva, A. A Real-World Size Organization of Object Responses in Occipitotemporal Cortex. *Neuron* **2012**, *74*, 1114–1124, doi:10.1016/j.neuron.2012.04.036.

8. Cichy, R. M.; Pantazis, D.; Oliva, A. Resolving human object recognition in space and time. *Nat. Neurosci.* **2014**, *17*, 455–462, doi:10.1038/nn.3635.

9. Cichy, R. M.; Pantazis, D.; Oliva, A. Similarity-Based Fusion of MEG and fMRI Reveals Spatio-Temporal Dynamics in Human Cortex During Visual Object Recognition. *Cereb. Cortex* **2016**, *26*, 3563–3579, doi:10.1093/cercor/bhw135.

10. Dale, A. M.; Halgren, E. Spatiotemporal mapping of brain activity by integration of multiple imaging modalities. *Curr. Opin. Neurobiol.* **2001**, *11*, 202–208, doi:10.1016/S0959-4388(00)00197-5.

11. Debener, S.; Ullsperger, M.; Siegel, M.; Engel, A. K. Single-trial EEG–fMRI reveals the dynamics of cognitive function. *Trends Cogn. Sci.* **2006**, *10*, 558–563, doi:10.1016/j.tics.2006.09.010.

461 12. Rosa, M. J.; Daunizeau, J.; Friston, K. J. EEG-fMRI INTEGRATION: A CRITICAL REVIEW OF
462   BIOPHYSICAL MODELING AND DATA ANALYSIS APPROACHES. *J. Integr. Neurosci.* **2010**, *09*,
463   453–476, doi:10.1142/S0219635210002512.

464 13. Huster, R. J.; Debener, S.; Eichele, T.; Herrmann, C. S. Methods for Simultaneous EEG-fMRI:
465   An Introductory Review. *J. Neurosci.* **2012**, *32*, 6053–6060, doi:10.1523/JNEUROSCI.0447-
466   12.2012.

467 14. Jorge, J.; van der Zwaag, W.; Figueiredo, P. EEG–fMRI integration for the study of human
468   brain function. *NeuroImage* **2014**, *102*, 24–34, doi:10.1016/j.neuroimage.2013.05.114.

469 15. Sui, J.; Adali, T.; Yu, Q.; Chen, J.; Calhoun, V. D. A review of multivariate methods for
470   multimodal fusion of brain imaging data. *J. Neurosci. Methods* **2012**, *204*, 68–81,
471   doi:10.1016/j.jneumeth.2011.10.031.

472 16. Khaligh-Razavi, S.-M.; Cichy, R. M.; Pantazis, D.; Oliva, A. Tracking the Spatiotemporal Neural
473   Dynamics of Real-world Object Size and Animacy in the Human Brain. *J. Cogn. Neurosci.*
474   **2018**, *30*, 1559–1576, doi:10.1162/jocn_a_01290.

475 17. Mohsenzadeh, Y.; Qin, S.; Cichy, R. M.; Pantazis, D. Ultra-Rapid serial visual presentation
476   reveals dynamics of feedforward and feedback processes in the ventral visual pathway. *eLife*
477   **2018**, *7:e36329*, 1–23, doi:https://doi.org/10.7554/eLife.36329.

478 18. Hebart, M. N.; Bankson, B. B.; Harel, A.; Baker, C. I.; Cichy, R. M. The representational
479   dynamics of task and object processing in humans. *eLife* **2018**, *7:e32816*, 1–22,
480   doi:https://doi.org/10.7554/eLife.32816.

481 19. Thorpe, S.; Fize, D.; Marlot, C. Speed of processing in the human visual system. *Nature* **1996**,
482   520–522.

483 20. VanRullen, R.; Thorpe, S. J. The Time Course of Visual Processing: From Early Perception to
484   Decision-Making. *J. Cogn. Neurosci.* **2001**, *13*, 454–461, doi:10.1162/08989290152001880.

485 21. Mormann, F.; Kornblith, S.; Quiroga, R. Q.; Kraskov, A.; Cerf, M.; Fried, I.; Koch, C. Latency
486   and Selectivity of Single Neurons Indicate Hierarchical Processing in the Human Medial
487   Temporal Lobe. *J. Neurosci.* **2008**, *28*, 8865–8872, doi:10.1523/JNEUROSCI.1640-08.2008.

488 22. Liu, H.; Agam, Y.; Madsen, J. R.; Kreiman, G. Timing, Timing, Timing: Fast Decoding of Object
489   Information from Intracranial Field Potentials in Human Visual Cortex. *Neuron* **2009**, *62*, 281–
490   290, doi:10.1016/j.neuron.2009.02.025.

491 23. Isik, L.; Meyers, E. M.; Leibo, J. Z.; Poggio, T. The dynamics of invariant object recognition in
492   the human visual system. *J. Neurophysiol.* **2014**, *111*, 91–102, doi:10.1152/jn.00394.2013.

493 24. Carlson, T.; Tovar, D. A.; Alink, A.; Kriegeskorte, N. Representational dynamics of object
494   vision: The first 1000 ms. *J. Vis.* **2013**, *13*, 1–1, doi:10.1167/13.10.1.

495 25. Contini, E. W.; Wardle, S. G.; Carlson, T. A. Decoding the time-course of object recognition in
496   the human brain: From visual features to categorical decisions. *Neuropsychologia* **2017**, *105*,
497   165–176, doi:10.1016/j.neuropsychologia.2017.02.013.

498 26. Simmons, J. P.; Nelson, L. D.; Simonsohn, U. False-Positive Psychology: Undisclosed Flexibility
499   in Data Collection and Analysis Allows Presenting Anything as Significant. *Psychol. Sci.* **2011**,
500   *22*, 1359–1366, doi:10.1177/0956797611417632.

501 27. Pashler, H.; Harris, C. R. Is the Replicability Crisis Overblown? Three Arguments Examined.
502   *Perspect. Psychol. Sci.* **2012**, *7*, 531–536, doi:10.1177/1745691612463401.

503 28. Bennett, C. M.; Miller, M. B. fMRI reliability: Influences of task and experimental design.
504   *Cogn. Affect. Behav. Neurosci.* **2013**, *13*, 690–702, doi:10.3758/s13415-013-0195-1.
505 29. Kanwisher, N.; McDermott, J.; Chun, M. M. The Fusiform Face Area: A Module in Human
506   Extrastriate Cortex Specialized for Face Perception. *J. Neurosci.* **1997**, *17*, 4302–4311,
507   doi:10.1523/JNEUROSCI.17-11-04302.1997.
508 30. Epstein, R.; Harris, A.; Stanley, D.; Kanwisher, N. The Parahippocampal Place Area:
509   Recognition, Navigation, or Encoding? *Neuron* **1999**, *23*, 115–125.
510 31. Epstein, R.; Kanwisher, N. A cortical representation of the local visual environment. *Nature*
511   **1998**, *392*, 598–601, doi:10.1038/33402.
512 32. Downing, P. E. A Cortical Area Selective for Visual Processing of the Human Body. *Science*
513   **2001**, *293*, 2470–2473, doi:10.1126/science.1063414.
514 33. Grill-Spector, K.; Kushnir, T.; Edelman, S.; Avidan, G.; Itzchak, Y.; Malach, R. Differential
515   Processing of Objects under Various Viewing Conditions in the Human Lateral Occipital
516   Complex. *Neuron* **1999**, *24*, 187–203, doi:10.1016/S0896-6273(00)80832-6.
517 34. Dilks, D. D.; Julian, J. B.; Paunov, A. M.; Kanwisher, N. The Occipital Place Area Is Causally and
518   Selectively Involved in Scene Perception. *J. Neurosci.* **2013**, *33*, 1331–1336,
519   doi:10.1523/JNEUROSCI.4081-12.2013.
520 35. Torralba, A.; Oliva, A. Statistics of natural image categories. *Netw. Comput. Neural Syst.* **2003**,
521   *14*, 391–412, doi:10.1088/0954-898X_14_3_302.
522 36. Bainbridge, W. A.; Oliva, A. A toolbox and sample object perception data for equalization of
523   natural images. *Data Brief* **2015**, *5*, 846–851, doi:10.1016/j.dib.2015.10.030.
524 37. Deng, J.; Dong, W.; Socher, R.; Li, L.-J.; Li, K.; Fei-Fei, L. ImageNet: A Large-Scale Hierarchical
525   Image Database. *IEEE Conf. Comput. Vis. Pattern Recognit.* **2009**, 8,
526   doi:10.1109/CVPR.2009.5206848.
527 38. Kriegeskorte, N. Representational similarity analysis – connecting the branches of systems
528   neuroscience. *Front. Syst. Neurosci.* **2008**, doi:10.3389/neuro.06.004.2008.
529 39. Kriegeskorte, N.; Kievit, R. A. Representational geometry: integrating cognition, computation,
530   and the brain. *Trends Cogn. Sci.* **2013**, *17*, 401–412, doi:10.1016/j.tics.2013.06.007.
531 40. John, L. K.; Loewenstein, G.; Prelec, D. Measuring the Prevalence of Questionable Research
532   Practices With Incentives for Truth Telling. *Psychol. Sci.* **2012**, *23*, 524–532,
533   doi:10.1177/0956797611430953.
534 41. Maxwell, S. E.; Lau, M. Y.; Howard, G. S. Is psychology suffering from a replication crisis?
535   What does "failure to replicate" really mean? *Am. Psychol.* **2015**, *70*, 487–498,
536   doi:10.1037/a0039400.
537 42. Munafò, M. R.; Nosek, B. A.; Bishop, D. V. M.; Button, K. S.; Chambers, C. D.; Percie du Sert,
538   N.; Simonsohn, U.; Wagenmakers, E.-J.; Ware, J. J.; Ioannidis, J. P. A. A manifesto for
539   reproducible science. *Nat. Hum. Behav.* **2017**, *1*, 0021, doi:10.1038/s41562-016-0021.
540 43. Haynes, J.-D.; Rees, G. Decoding mental states from brain activity in humans. *Nat. Rev.*
541   *Neurosci.* **2006**, *7*, 523–534, doi:10.1038/nrn1931.
542 44. Grill-Spector, K.; Malach, R. THE HUMAN VISUAL CORTEX. *Annu. Rev. Neurosci.* **2004**, *27*,
543   649–677, doi:10.1146/annurev.neuro.27.070203.144220.
544 45. Op de Beeck, H. P.; Haushofer, J.; Kanwisher, N. G. Interpreting fMRI data: maps, modules
545   and dimensions. *Nat. Rev. Neurosci.* **2008**, *9*, 123–135, doi:10.1038/nrn2314.

546 46. Amano, K. Estimation of the Timing of Human Visual Perception from
547   Magnetoencephalography. *J. Neurosci.* **2006**, *26*, 3981–3991, doi:10.1523/JNEUROSCI.4343-
548   05.2006.
549 47. Ioannidis, J. P. A. Why Most Published Research Findings Are False. *PLoS Med.* **2005**, *2*, 6.
550 48. Button, K. S.; Ioannidis, J. P. A.; Mokrysz, C.; Nosek, B. A.; Flint, J.; Robinson, E. S. J.; Munafò,
551   M. R. Power failure: why small sample size undermines the reliability of neuroscience. *Nat.*
552   *Rev. Neurosci.* **2013**, *14*, 365–376, doi:10.1038/nrn3475.
553 49. Riesenhuber, M.; Poggio, T. Neural mechanisms of object recognition. *Curr. Opin. Neurobiol.*
554   **2002**, *12*, 162–168, doi:10.1016/S0959-4388(02)00304-5.
555 50. Serre, T.; Oliva, A.; Poggio, T. A feedforward architecture accounts for rapid categorization.
556   *Proc. Natl. Acad. Sci.* **2007**, *104*, 6424–6429, doi:10.1073/pnas.0700622104.
557 51. Caceres, A.; Hall, D. L.; Zelaya, F. O.; Williams, S. C. R.; Mehta, M. A. Measuring fMRI
558   reliability with the intra-class correlation coefficient. *NeuroImage* **2009**, *45*, 758–768,
559   doi:10.1016/j.neuroimage.2008.12.035.
560 52. Miller, M. B.; Van Horn, J. D. Individual variability in brain activations associated with
561   episodic retrieval: A role for large-scale databases. *Int. J. Psychophysiol.* **2007**, *63*, 205–213,
562   doi:10.1016/j.ijpsycho.2006.03.019.
563 53. Taulu, S.; Kajola, M.; Simola, J. Suppression of Interference and Artifacts by the Signal Space
564   Separation Method. *Brain Topogr.* **2003**, *16*, 269–275,
565   doi:10.1023/B:BRAT.0000032864.93890.f9.
566 54. Taulu, S.; Simola, J. Spatiotemporal signal space separation method for rejecting nearby
567   interference in MEG measurements. *Phys. Med. Biol.* **2006**, *51*, 1759–1768,
568   doi:10.1088/0031-9155/51/7/008.
569 55. Tadel, F.; Baillet, S.; Mosher, J. C.; Pantazis, D.; Leahy, R. M. Brainstorm: A User-Friendly
570   Application for MEG/EEG Analysis. *Comput. Intell. Neurosci.* **2011**, *2011*, 1–13,
571   doi:10.1155/2011/879716.
572 56. Kriegeskorte, N.; Goebel, R.; Bandettini, P. Information-based functional brain mapping. *Proc.*
573   *Natl. Acad. Sci.* **2006**, *103*, 3863–3868, doi:10.1073/pnas.0600244103.
574 57. Haynes, J.-D.; Sakai, K.; Rees, G.; Gilbert, S.; Frith, C.; Passingham, R. E. Reading Hidden
575   Intentions in the Human Brain. *Curr. Biol.* **2007**, *17*, 323–328, doi:10.1016/j.cub.2006.11.072.
576 58. Wang, L.; Mruczek, R. E. B.; Arcaro, M. J.; Kastner, S. Probabilistic Maps of Visual Topography
577   in Human Cortex. *Cereb. Cortex* **2015**, *25*, 3911–3931, doi:10.1093/cercor/bhu277.
578 59. Maris, E.; Oostenveld, R. Nonparametric statistical testing of EEG- and MEG-data. *J. Neurosci.*
579   *Methods* **2007**, *164*, 177–190, doi:10.1016/j.jneumeth.2007.03.024.
580 60. Pantazis, D.; Nichols, T. E.; Baillet, S.; Leahy, R. M. A comparison of random field theory and
581   permutation methods for the statistical analysis of MEG data. *NeuroImage* **2005**, *25*, 383–
582   394, doi:10.1016/j.neuroimage.2004.09.040.